ADVANCED FUNCTIONAL MATERIALS
www.afm-journal.de

Charge Transport in Highly Heterogeneous Natural Carbonaceous Materials

Huashan Li, Taishan Zhu, Nicola Ferralis, and Jeffrey C. Grossman**

Natural carbonaceous materials (NCMs) have recently emerged as promising organic semiconducting materials for electronics and catalysis, although the fundamental picture of charge transport within NCM systems is still incomplete. Morphologically, NCMs exhibit reminiscence of disordered organic solids, yet the experimental measurements demonstrate a transport regime that surprisingly follows Mott's formula derived for variable-range hopping in inorganic noncrystalline materials. With ab initio and kinetic Monte Carlo simulations, a temperature scaling is revealed between the Gaussian-defect model $\log(\sigma) \sim T^{-2}$ typical for organic matter and the Mott-like $\log(\sigma) \sim T^{-1/4}$ for a wide spectrum of intermolecular connectivity. As dominant transport descriptors, energy levels and coupling strengths are screened among 30 small molecules with varying sizes, shapes, sp^2/sp^3 ratios, side chains, and functional groups. These analyses provide insight for the design of NCM electronics, and should also be applicable to disordered molecular materials in general.

1. Introduction

Carrier transport in materials exhibiting strong heterogeneity underlies many important scenarios, ranging from batteries[1] to thermoelectrics,[2] and from neuroscience[3] to oncology.[4] One notable example is natural carbonaceous materials (NCMs), such as coal, tar and pitch.[5] NCMs are earth-abundant and processing-friendly, and have gained attention as alternative carbon sources, such as for carbon fibers,[6] or for electronic applications.[7] For instance, through a simple annealing process, the electrical conductivity of sintered coal nanoparticles was tuned by seven orders of magnitude, and electronic gap was varied from 0 to 1.8 eV.[7] Such a wide range of tunability typical for astrophysics is relatively rare for solid-state physics, especially considering the highly heterogeneous nature of the studying material. The diverse chemistry of coal was also utilized to produce fluorescent carbon quantum dots (QDs),[8] with potential applications in chemical sensing[8b] and photocatalytic activity.[8c] While this initial research certainly hints to further opportunities for electronic applications, the wider adaption of NCMs is limited by a lack of corresponding structure–properties–processing relations.

The modeling challenges of mapping atomistic structures to measurable properties for heterogeneous media can be primarily identified in the lack of: (i) microscopic structural models and (ii) charge transport models. The microscopic representation is generally unavailable for cross-linked defect-free networks. This is particularly true for NCMs,[9] since the NCM family encompasses a full spectrum of complex morphologies and chemistries obtained across geological timescales. For this purpose, we have developed a numerical protocol to generate representative atomistic systems for NCM networks (Methods section, Supporting Information). Yet, even in presence of structural models, consistent charge transport theories for disordered materials, despite decades of extensive research, are still missing, in contrast to the band theory and kinetic models for crystalline materials.[10] Historically, various phenomenological models have been derived based on incoherent hopping between localized states,[11] and applied to amorphous inorganic semiconductors,[12] colloidal quantum dots,[13] doped polymers, and organic molecule assemblies.[14] However, thus far very limited theories common to different disordered materials have been developed. For instance, for purely amorphous systems, the energy spectrum and wavefunction structure near mobility edges that are expected to dominate transport are mostly hypothesized for nearly all disordered materials and believed to have different functional forms.[10,11] The exponential form that usually applies in inorganic amorphous materials leads to the well-known Mott's formula for carrier mobility, $\log(\mu) \approx T^{-1/4}$ scaling behavior, whereas the Gaussian form that often applies to disordered organic materials gives rise to a $\log(\mu) \approx T^{-2}$ dependence. The nonpurely amorphous nature of NCMs, with the inclusion of chemically well-defined molecular fragments with varying size,[5] shape, and functionality, leads to the carrier energy spectrum of NCMs being composed of discrete localized states. In addition, due to the local structures in NCMs explained in the following, intercarrier coupling would be of crucial importance for their transport properties. Moreover, the ultrasensitivity of

Prof. H. Li
School of Physics
Sun Yat-sen University
Guangzhou 510275, China
E-mail: lihsh25@mail.sysu.edu.cn
Prof. H. Li, Dr. T. Zhu, Dr. N. Ferralis, Prof. J. C. Grossman
Department of Materials Science and Engineering
Massachusetts Institute of Technology
Cambridge, MA 02139, USA
E-mail: jcg@mit.edu
The ORCID identification number(s) for the author(s) of this article can be found under https://doi.org/10.1002/adfm.201904283.

DOI: 10.1002/adfm.201904283

carrier mobility in organic materials has been observed to type and degree of molecular disorder (e.g., diagonal vs off-diagonal, fragment size/shape, molecular packing), charge-carrier density, and extrinsic environment (e.g., temperature, pressure, and electric field).[10] While theories are under development, insights from accurate simulations are currently valuable, yet rare due to computational complexities.

In this work, we bridge this gap by establishing a link between local molecular structure and global charge transport via phonon-assisted hopping in NCMs. In lieu of all four coal systems previously experimentally studied in the context of establishing the charge transport characteristics,[7] here we focus on a high volatile A sub-bituminous coal sample from the Penn State Coal Bank (DECS 31, Kimper, Pike County Kentucky, USA). Based on the measured molecular fingerprints for hvAb[15] and the measured Raman spectra (**Figure 1**a), we construct 16 NCM systems traversing a range of aromatic and aliphatic fragments, bridges, side chains, and degrees of connectivity to: (i) fully scan the structural phase space (Figure 1b–d) using molecular dynamics (MD) simulations and (ii) predict the electronic structure within density functional theory, and calculate the carrier mobility by kinetic Monte Carlo (details available in the Experimental Section and Section SA and SB, Supporting Information). Both the fragment size (about ten aromatic rings) and the H/C, O/C ratios are chosen to align with the hvAb coal sample in previous experiments.[7] Only C, H, and O were considered in the transport calculations for simplicity, while the influences of S and N were included during the screening of isolated molecules and dimers. The connectivities are established via direct C—C bonding or bridging by C, O, C—C, C—O, while the remaining O are in the form of OH, COOH, C_5O, C_4O functional groups, as suggested by reported measurements[16] and coal models.[17] These systems with varying microscopic structure features as seen from the radial/angle distribution functions (Figure 1e,f) are summarized in **Table 1**. Using first-principles approaches, we calculated 30 systems in a high-throughput fashion to transverse different systems that are representative of known microstructures in

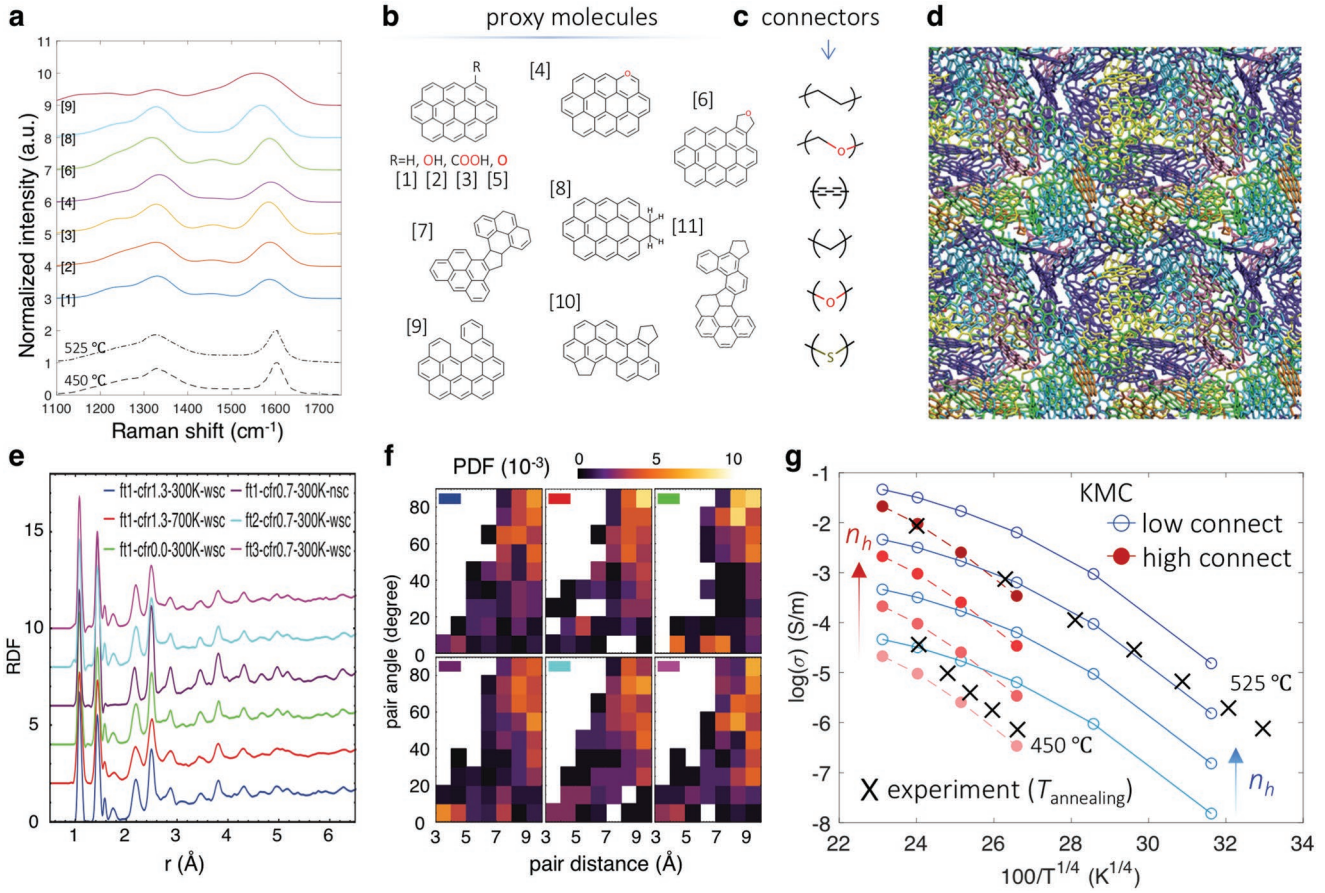

Figure 1. Microscopic representation and electrical conductivity of NCMs. a) Raman spectra for coal samples annealed at 450 and 525 °C compared to b,c) DFT calculations for proxy molecules. d) One of the samples composed of proxy molecules and molecular connectors. With these molecular fragments and connectors, various confirmations could be realized, including closely and loosely packed systems with high and low intermolecular connectivities. 16 representative systems are summarized in Table 1. e) Radial distribution function (RDF) of samples with various sets of fragment type and connectivity to fragment ratios (cfr) including/excluding side chains (wsc/nsc) at different temperatures. Artificial offsets on the *y*-axis are placed between plots for easier comparison between samples. f) Probability density histograms of distances and angles of fragment pairs. g) Electrical conductivity σ from experiment and ab initio simulations. Both closely packed (NCM 4, red lines) and loosely packed (NCM 2, blue lines) systems are shown. Charge density varies from 10^{13} cm^{-3} at the bottom to 10^{16} cm^{-3} at the top. While the numerical results of closely packed system agree with experiments, the less packed system shows a different scaling behavior $T^{-3/2}$.

Table 1. Structural information on the samples selected for charge transfer rate analysis within each type of NCM. "O form" means the chemical groups containing O atoms within fragments, n_b/n_f denotes the ratio of bridge number to fragment number. $C_8/2C_8$ stands for one/two alkyl side chains containing eight C atoms. Bridge type C_2 means direct connectivity between two C anchors, C_n indicates the bridge is composed of (n–2) C atoms.

NCM	Frag type	Side chain	Connectivity	H/C	O/C	n_b/n_f
1	1	C_8	None	0.750	0.000	0.00
2	1	C_8	C_2, C_3, COC	0.726	0.002	0.33
3	1	C_8	C_2, C_3, COC	0.699	0.006	0.66
4	1	C_8	C_2, C_3, COC	0.655	0.011	1.32
5	1	None	C_2, C_3, COC	0.386	0.005	0.66
6	1	C_8	C_4, COC_2	0.724	0.009	0.66
7	1,2,3,4	C_8, $2C_8$	None	0.766	0.054	0.00
8	1,2,3,4	C_8, $2C_8$	C_2, C_3, COC	0.729	0.054	0.33
9	1,2,3,4	C_8, $2C_8$	C_2, C_3, COC	0.716	0.054	0.66
10	1,2,3,4	C_8, $2C_8$	C_2, C_3, COC	0.676	0.060	1.32
11	1,2,3,4	None	None	0.432	0.061	0.00
12	1,2,3,4	None	C_2, C_3, COC	0.407	0.069	0.33
13	1,2,3,4	None	C_2, C_3, COC	0.388	0.063	0.66
14	1,2,3,4	C_8, $2C_8$	C_2, C_3, COC, C_4, COC_2	0.769	0.043	0.33
15	3,5,6,7	C_8, $2C_8$	C_2, C_3, COC	0.753	0.050	0.33
16	1,8,9,10,11	C_8	C_2, C_3, COC	0.789	0.003	0.33

NCMs. Note that the static change of molecular geometry due to local connectivity has also been taken into account for electronic calculations.

2. Results and Discussion

2.1. Carrier Mobility and Tunability Space

We start by noticing both quantitative agreement and intriguing deviations between previously reported experiments[7] and computational results of effective conductivity (Figure 1h). On the one hand, the numerical results for a highly connected system (NCM 4 with the ratio of bridge number to fragment number $n_b/n_f = 1.32$, red lines in Figure 1g) with charge density varying from 10^{13} to 10^{16} cm^{-3} are in good agreement with the earlier experimental measurements for systems annealed at low temperatures (425 and 520 °C).[7] A $\log(\sigma) \sim T^{-1/4}$ temperature dependence can be observed for these closely packed systems. On the other hand, given the molecular nature of NCM building blocks, it is still surprising that the temperature scaling coincides with Mott's formula derived initially for doped inorganic semiconductors. Instead, for organic material systems, a wide range between $T^{-1/4}$ and T^{-3} has been reported for different materials, depending on composition chemistry and crystallinity.[10] To understand this discrepancy, less interconnected systems were studied (e.g., NCM 2 with n_b/n_f = 0.33, blue lines in Figure 1g). For NCM 2, the scaling is $T^{-3/2}$. Interestingly, such scaling behavior, observed in both NCM 2 and NCM 4, falls between the Mott and Gaussian-defect limits.

Note that the power-law scaling $\log(\sigma) \sim T^{-n}$, $n \in [0.5, 3]$ derives from charge–phonon coupling in crystals. For highly disordered materials, as in this case, rigorous theories are still under development. Empirical formulations, such as the Arrhenius-type $\log(\sigma) \sim T^{-1}$ and Gaussian-type $\log(\sigma) \sim T^{-2}$, have been extensively used to fit experimental data in the literatures, examples including polyparaphenylene vinylene (PPV) derivatives,[18] poly-3-hexylthiophene (P3HT),[19] and calamitic liquid crystals.[20] The former is consistent with the multiple trapping and release (MTR) model with homogeneously dispersed traps, as a special case of the more general continuous time random walk (CTRW) model by Scher and Lax.[10] In this picture, transport operates via a succession of trapping events and thermal releases. However, it is worth noting that no theoretical justification for the Arrhenius law exists. In contrast, the latter Gaussian type was obtained by fitting Monte Carlo simulations in the presence of a site-energy disorder from a normal distribution.[10]

Interestingly, the simulations of NCM presented here show the coexistence of both types of transport mechanisms: (i) energy distributions in our systems resemble Gaussians; (ii) with increasing interconnectivity, we observed severe carrier trapping, which suggests the presence of trapping sites deeper than $k_B T_c$ (**Figure 2**a). For NCM 2, kinetic Monte Carlo (KMC) results appear to be in between the two regimes ($n = 1.5$), which we thus attribute to the coexistence of charge trapping and energetic disorder. When individual fragments are tightly linked, the molecular character is expected to diminish gradually and trap–detrap behaviors exhibited by close-packing inorganic amorphous semiconductors should emerge and dominate, leading to the Mott-type scaling $\log(\sigma) \sim T^{-1/4}$. In other words, $n = 1/4$ is the lower bound for our tightly connected organic NCM systems. Therefore, the interplay between site trapping and energetic disorder explains the observed scaling change from $n = 1.5$ to $n = 1/4$. The increased discrepancy between computational and experimental data at high operational temperatures may arise from the collective excitation of delocalized carriers, which has not been evaluated in our model due to the small proportion of conjugating connectivity within the NCM network, and the formidable complexity of tracing charge transport through undeterministic fragments. These results indicate that systems with a full spectrum of connectivities and packing densities could be realized experimentally at different annealing temperatures, benefitting from the native, chemically diverse range of molecular fractions in NCM.

2.2. Molecular Descriptors of Transport Properties

The range of structural parameters defining the tunability of the energy profile, electron coupling, charge hopping rate, and transition imbalance were explored using representative molecular networks as shown in Table 1. The effects of varying fragments could be obtained by comparing NCM 1–6 to NCM 7–14, while the influences of connectivities between fragments are probed within each category. To establish the link between structural and transport properties, we assess the critical transport variables that govern charge transport in disordered materials: (i) the driving force, dG, defined as

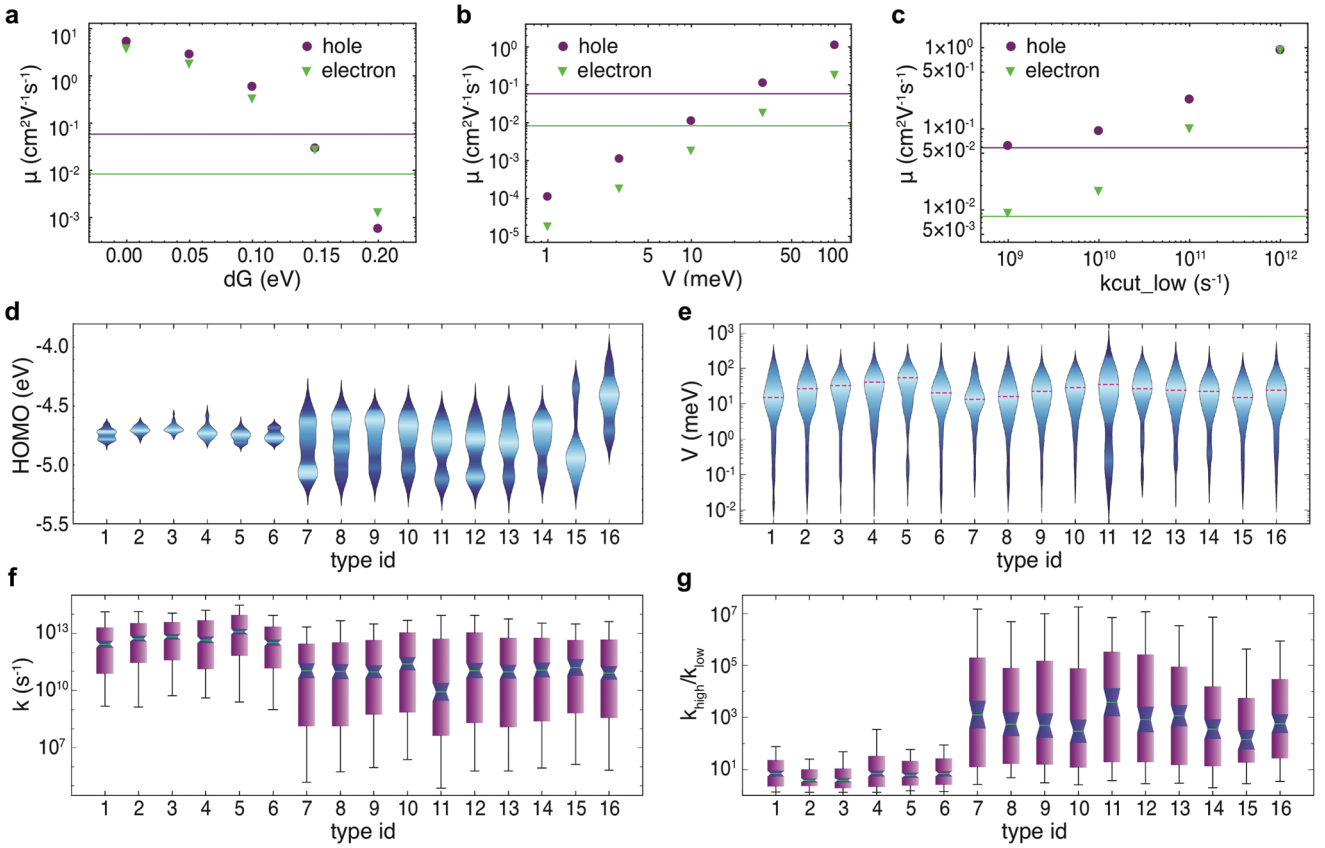

Figure 2. Dependence of transport variable distribution on network configuration. Carrier mobility μ of a NCM 4 sample with the a) absolute values of driving force $|dG|$ for all pairs made to be identical, b) electron couplings V for all pairs replaced by identical values, c) hopping rates k for the pairs with ($k < k_{cut\_low}$) replaced by k_{cut_low}. k_{cut_low} is a variable introduced to define slow charge hopping channels. The horizontal lines denote μ of the original system. Probability density functions (PDF) of d) highest occupied molecular orbital (HOMO) and e) V between HOMOs for samples of various types. The values of PDF are illustrated by the widths of the patterns and correlated to the color brightness, with the dashed red lines highlighting the largest probability. Box-and-whisker charts of f) hopping rate and g) transition imbalance defined as the ratio between the larger and smaller value among forward and backward hopping rates (k_{high}/k_{low}) for hole transport in samples of various types calculated at 300 K, with the median illustrated by the green central marker line, the 25/75% quantile presented by the box, and the 10/90% quantile denoted by the lower/upper fence.

the energy change during transition process; (ii) reorganization energy, λ, which is the energy drop caused by relaxation of final electronic state from initial equilibrium geometry; and (iii) electron coupling, V, which quantifies the wavefunction overlap between initial and final states. In general, hopping rate, k and thus carrier mobility, μ of a network composed of identical components could be enhanced by decreasing dG and λ, and increasing V.[21] While dynamic disorder stemming from nonlocal electron–phonon coupling has been demonstrated to reduce charge mobility by over 50% at high temperature, the exclusion of such an effect still leads to a reasonable prediction of the trend in temperature-dependent mobilities.[22] Within the goal set for this work to understand the impact of spatial disorder induced by a complex network that is absent in molecular crystals (along with the formidable computational load), variations of electron–phonon coupling with respect to time and chemical environment have not been accounted in this study. Thus, the following discussion will focus on the distribution of transport variables dG and V (with λ of various types of fragments documented in Section SC, Supporting Information).

As shown in Figure 2a–c, we found carrier mobility μ to be highly sensitive to transport variables by orders of magnitude. In particular, μ is extremely sensitive to the driving force $|dG|$, with a four orders of magnitude enhancement in μ by reducing $|dG|$ from 0.2 to 0.0 eV (Figure 2a). Despite the fact that a majority of $|dG|$ are below 0.1 eV, our prototype network with a distribution of $|dG|$ exhibits much lower μ than that of the network with identical $|dG| = 0.1$ eV, illustrating the detrimental effect of large fluctuations in $|dG|$ and consequential charge trapping, even in limited portions of the energy landscape. This is consistent with the inefficient charge transport in NCMs compared to that in synthetic organic systems with relatively homogeneous chemical environments. Similarly, a broad distribution of the electron coupling ranging from 0.01 to 300 meV in the original sample leads to μ that is comparable to the network with an identical value $V = 20$ meV (Figure 2b). Based on the above observations, reducing eigenvalue fluctuations to within 0.1 eV and increasing electron coupling to 50–100 meV may lead to $\mu > 1$ cm^2 V^{-1} s^{-1}. Such findings highlight the essential impact of the distributions (rather than average values) of transport variables on transport properties,

for highly disordered systems such as NCM considered in this study. Further we explore the influence of the distribution in hopping rates k on μ by controlling the upper and lower boundaries (replacing the values beyond the range by the nearby boundaries) while keeping the geometry of the reference network. As expected, μ can be substantially increased by modifying low k components (Figure 2c), which is consistent with the general view that the elimination of trap states is crucial for improving transport properties. In addition, the presence of extremely high k is not necessary to achieve high μ. Instead, maintaining a balance between forward and backward hopping is more important in these materials (Figure S4, Supporting information).

The distribution of energy levels in NCMs depends strongly on the fragments and connectivities (Figure 2d). Increasing the ratio of number of connectivities to that of fragments from 0.0 to 1.3 (NCM 1 to 4, NCM 7 to 10, Table 1) results in a nonmonotonic change of energy level broadening. In other words, both low and high degrees of connectivity lead to relatively rough energy landscapes. This stems from the connectivity affecting the energy level distributions in different ways: (i) suppression of aggregations driven by π–π stacking that may cause large structural distortion; (ii) increase of structural fluctuations of fragments constrained by connectivity; (iii) smoothing of the overall energy profile of the ensemble by enhancing overlap between eigenvalue distributions associated with different fragment types. Excluding side chains (NCM 3 vs 5, NCM 7–9 vs 11–13, Table 1) slightly affects the energy profile via strengthening π–π stacking, which arises from the weaker steric repulsion and results in larger fragment distortions. Variation of fragment types by tuning molecular shape and functional group (NCM 2 vs 8 vs 15 vs 16, Table 1) leads to significantly different energy landscapes as expected from the distinct energy levels of fragment types. Similarly, the electron coupling distribution can also be adjusted by these structural parameters (Figure 2e). V, as expected, is decreased by the introduction of long bridges (NCM 6 vs 3, Table 1). Both a higher degree of connectivity and exclusion of side chains provide larger V. While the former can be explained by the promoted tunneling via a super-exchange mechanism, the latter is ascribed to the enhanced V by stronger π–π interactions.

For each network type (Table 1), we further investigated the pairwise charge transfer rate that measures the intrinsic capability for a carrier to hop through fragment interfaces, as well as the forward–backward transition ratio that unveils the possibility for it to get trapped by energetically favorable sites. The extension of hole hopping rates (Figure 2f) and forward–backward transition ratio (Figure 2g) over orders of magnitude reflects the highly disordered nature of NCM. The broadening of rate and imbalance distributions dramatically increases with the number of fragment types (NCM 1–6 vs 7–16) as a consequence of the widened energy level distribution. By contrast, the differences in rate and imbalance distribution between samples containing different types of fragments are relatively small compared to the remarkable diversity in their energy profiles, as long as the overall broadening of energy distribution is similar (NCM 8 vs 15 vs 16). Moreover, increasing the degree of connectivity leads to higher hopping rates and a lower transition imbalance, and thus favors transport in the low connectivity regions, while the opposite trend may be present in high connectivity regions due to the increasing roughness of the energy profile. The impact of side-chain and long-bridge connections on rate and imbalance cannot be easily predicted because the variations of dG and V strongly compete with each other. The above discussions on Figure 2 are associated with hole hopping, and a similar analysis for electron transport can be found in Figure S5 (Supporting information).

The sensitivity to variations and distributions of transport descriptors is essential for achieving optimal designs of NCM-based electronic devices. Therefore, we developed a set of key graphic descriptors composed of the distributions of μ, dG, V and their relationships for NCM 2 as presented in **Figure 3**a–d (justification of such descriptor is provided in Section SF, Supporting Information). The first and second graphs show the joint distribution of hopping rate and transport variables for connected and nonconnected fragment pairs (Figure 3a,b), indicating the existence and distribution of potential local transport paths, as well as the limiting factors to transition rates. The feasibility of these paths is shown in the third and fourth graphs (Figure 3c,d). The third graph depicts the probability density of the forward–backward transition ratio and its dependence on dG (Figure 3c), implying the possibilities for charge transport to be terminated by deep trap states. The fourth graph shows the number of available escape paths that reflects the degree of connectivity between local paths and thus the percolation feature of the global network (Figure 3d). Detailed transport descriptors for both holes and electrons are documented in Section SG (Supporting Information).

These findings at the molecular scale account well for the mobility trend observed in Figure 3i. The larger fluctuation of electron mobility compared to that of hole mobility can be explained by the higher sensitivity of lowest unoccupied molecular orbital (LUMO) distribution to morphology fluctuations. The degree of connectivity (NCM 1–4) has two major impacts on carrier transport: (1) modification of the distribution of driving force dG and the density of trap states (Figure 3g); and (2) introduction of more transport channels with high hopping rates (Figure 3e), at the cost of reducing coupling between other nonconnected pairs (Figure 3f). Consequently, a relatively high μ is achieved for a moderate degree of connectivity (Figure 3i). Exclusion of side chains (NCM 5 vs 3) results in closer π–π stacking and decreased number of effective hopping paths per site. The system without side chains exhibits a narrower highest occupied molecular orbital (HOMO) distribution (Figure 3g), which in combination with enhanced coupling (Figure 3f), leads to a slight improvement in hole mobility. By contrast, the LUMO distribution becomes much broader, and therefore electron mobility is remarkably suppressed by the large rate imbalance and reduced number of hopping paths. Despite the fact that electron couplings of fragments connected by long bridges are relatively smaller than those connected by short bridges (NCM 6 vs 3, Figure 3f), they are sufficient to provide high hopping rates (Figure 3e), and thus lead to similar hole mobilities. Alternatively, the substantially decreased electron mobility with longer bridges can be explained by the broadening of driving force distribution.

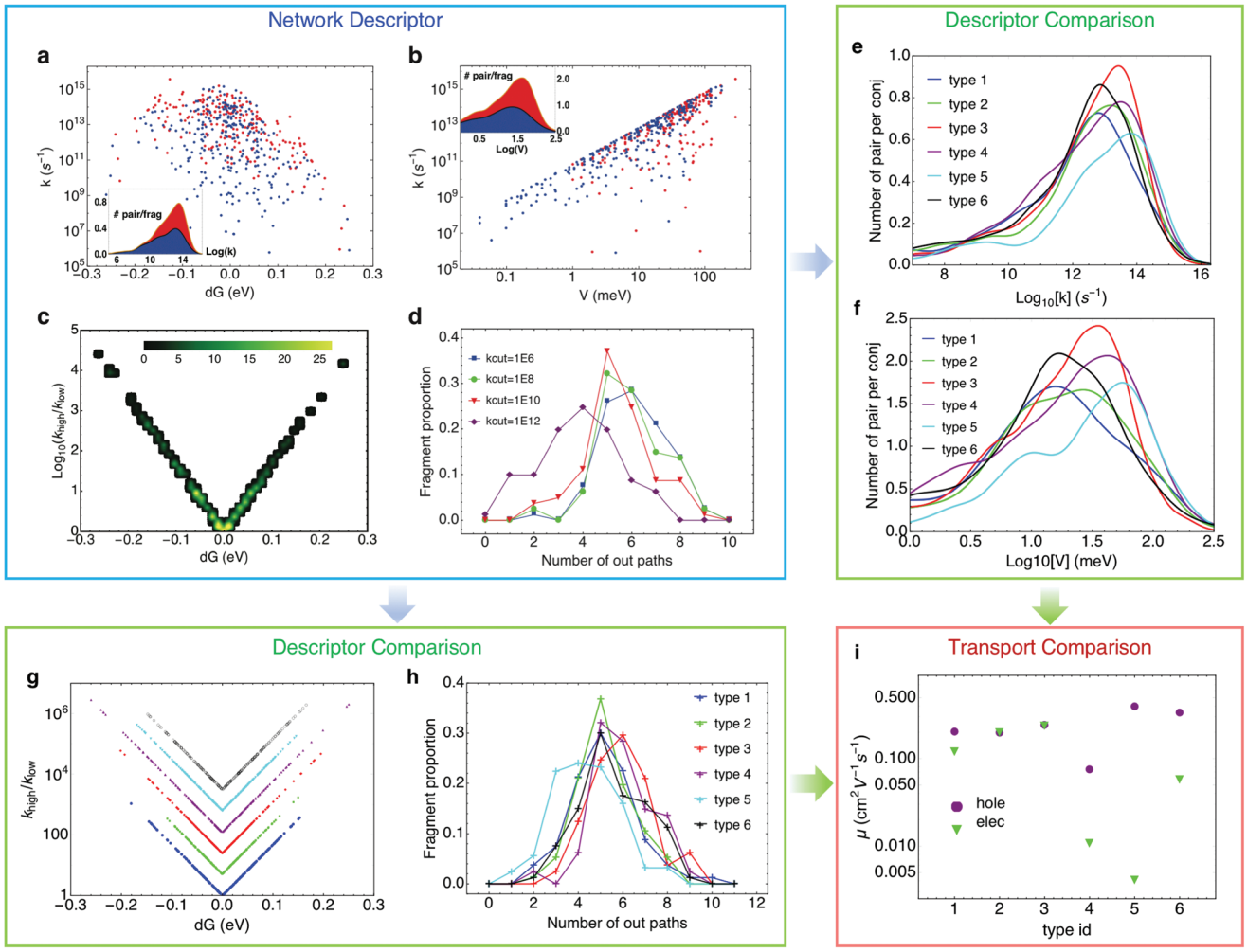

Figure 3. Relationship between molecular descriptors and transport properties in distribution representation. Characteristic graphs of NCM for charge transport with hole hopping of NCM 4 as an example: a) Joint distribution of k and dG for connected (in red) and nonconnected (in blue) pairs, with the inset showing the histogram of log(k) normalized by the total number of fragments. b) Joint distribution of k and V, with the inset showing the histogram of log(V). c) Joint distribution of transition imbalance and dG. d) Distributions of the number of paths for hopping away from a fragment, with the existence of a path judged by the criterion $k > k_{cut}$, where k_{cut} is the lower limit of the rates associated with the charge transfer events that are possible to happen compared to other processes. Comparisons of characteristic graphs between different types regarding hole hopping: distributions of e) log(k) and f) log(V) normalized by the total number of fragments, g) joint distributions of transition imbalance and dG, and h) distributions of the number of paths for hopping away from a fragment for different samples. The common reference points (0.0, 1.0) are artificially shifted for clarity in panel (g). i) Carrier mobilities of network NCM 1–6 at 300 K.

2.3. Screening Criteria for Fragments and Connectivities

While important for predicting transport properties, energy level and electron coupling distributions of the entire network are computationally much too demanding for throughput screening. Alternatively, information about each fragment and connectivity type may serve as low-level descriptors to enable a primary selection for narrowing down the optimization phase space in both theoretical and experimental explorations. For this purpose, we investigated the fluctuation of energy levels in response to change of size, shape, side chain, and functional group using a series of small molecules (**Figure 4**a, Figures S9 and S10, Supporting information). The high sensitivity of eigenvalues to structural variations unveils the broad energy level distribution of the network composed of various fragments, which is likely to be the essential reason for the low conductivity of most NCMs. Similar fragment shape within the entire ensemble is also necessary to provide a satisfactory energy profile with less than 0.1 eV eigenvalue fluctuations. Interestingly, substitutions of H by OH, C_5O, SH, and alkyl side chains have a negligible effect on the eigenvalues and thus are favorable for transport properties. Most of the remaining functional groups such as COOH, O, C_4O, C_5N, NH_2, and C_5S shift the eigenvalues dramatically and should be avoided in practice.

Despite that nonconnected fragments may dominate charge hopping, estimation of electron coupling for various types of connectivities is still of crucial importance. We attempted to interpret the dependence of V on interfacial configurations by sampling over 13 molecular fragment types with 2 orientations and 3 representative anchor points for each type (unrealistic structures

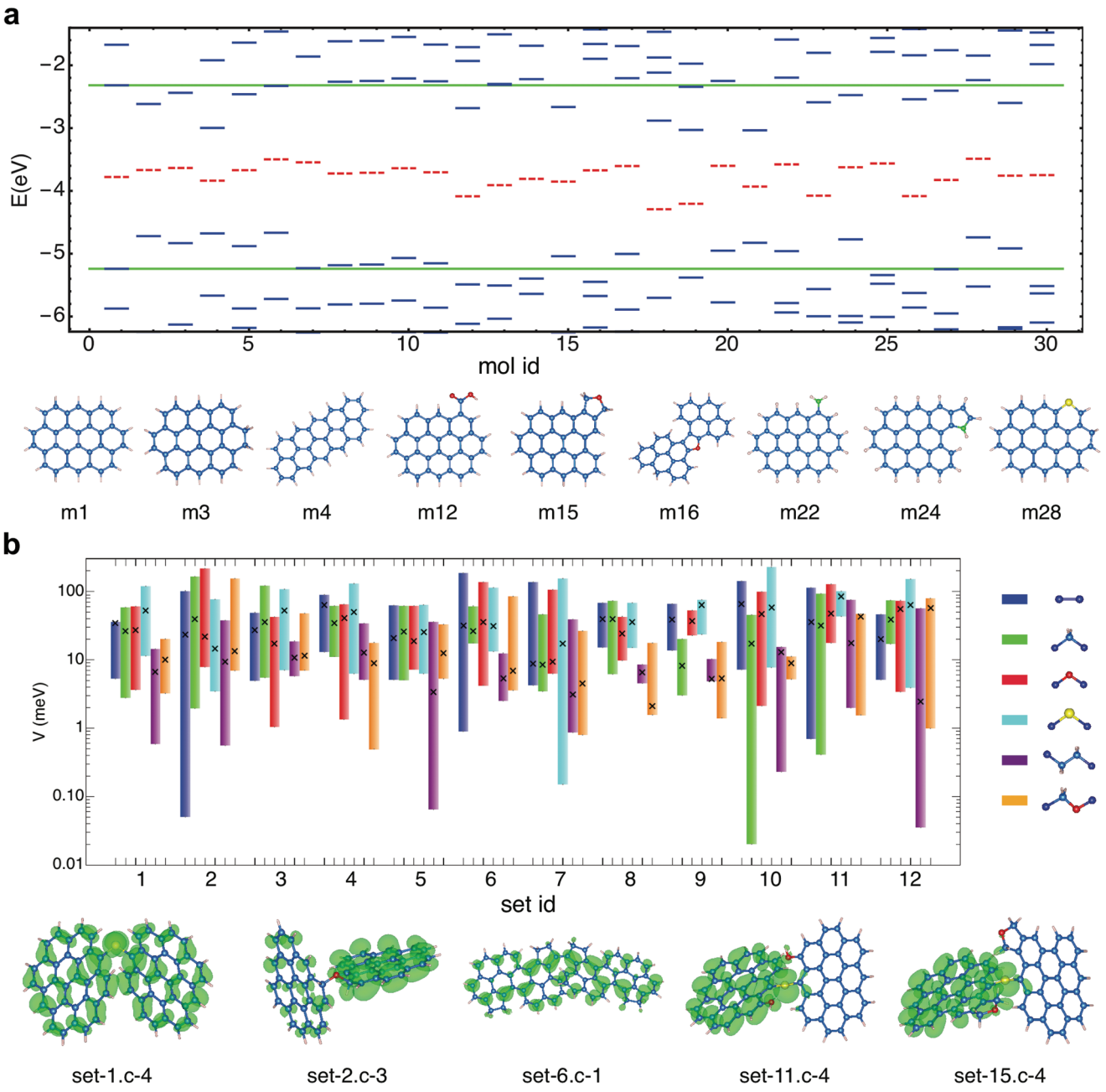

Figure 4. Screening of fragments and connectivities. a) The eigenvalues of 30 small molecular fragments with various sizes, shapes, sp^2/sp^3 ratios, side chains, and functional groups, with the middle of bandgap illustrated by red dashed lines. Representative molecule structures are shown with the color scheme—C: blue, H: pink, O: red, N: green, S: yellow. b) Distributions of electron coupling between HOMOs for different sets of molecular dimers with various connectivities, including direct C—C bonding and bridging with CH_2, O, S, C_2H_4, and OCH_2. The lower and upper boundaries of the bars correspond to the smallest and largest values among the set of samples, and the median is denoted by the cross marker. Dimer structures that are favorable for improving *V* are shown along with the HOMO wavefunctions, with the notation set-x.c-y meaning the sample with largest *V* among the set x with connectivity type y.

were discarded). Connections by short bridges (CH_2, O, S) or direct bonding provide much larger coupling than longer bridges, with values spanning, surprisingly, several orders of magnitude (10^{-1} to 10^2 meV) with different anchor points and orientations (Figure 4b, Figure S11, Supporting information). In general, large couplings arise from configurations where sp^2 domains are close to each other, or fragments are well-aligned taking advantage of the relatively small steric repulsion. Functional groups adjacent to the interface can assist wavefunction overlap and enhance coupling.

3. Conclusion

We note that our model requires additional complexity (e.g., including S and N elements in the network, predicting carrier

mobilities with appropriate techniques to handle deep trap states, taking into account partial coherent charge transfer, expanding the cell size and sampling density, etc.) for a more quantitative description of NCM systems. Nevertheless, the general and qualitative principles unveiled in this study are applicable to a wide range of NCM, and allow to computationally characterize the even broader categories of highly disordered materials. For example, biomaterials have demonstrated their outstanding efficiency and robustness for energy conversion processes, yet the potential of the entire family of highly disordered materials featured by intrinsic chemical and structural diversity and high tunability have not been fully explored.

In summary, we have developed an atomic-scale model to describe the charge transport in highly disordered NCMs. A temperature scaling between the Gaussian-defect model $\log(\sigma) \sim T^{-2}$ typical for organic matter and the Mott-like $\log(\sigma) \sim T^{-1/4}$ is observed for prototype networks with various intermolecular connectivities. Structure–property relation based on the distributions of transport variables is then established, leading to a new set of graphic descriptors for NCMs accounting the energy and coupling variations originating from severe inhomogeneity. The model of charge transport in NCMs provided in this work highlights how the chemical and structural complexity of NCM, often seen as a limitation in their use for technological applications, can offer a widely tunable platform for their use to develop novel applications in the sensing, biomedicine, and electronics using NCM as the active base material.

4. Experimental Section

Structural Evolution: Advanced bottom-up algorithms such as reverse Monte Carlo (RMC)[9,23] and Fringe3D (based on imaging analysis)[24] were developed to build microscopic models for natural carbon materials, which successfully reproduced adsorption, mass transport, and mechanical properties measured in experiments.[9] However, when considering electronic properties, the existence of artifacts associated with the imperfection of the force fields employed in these models can induce unrealistic trap states limiting their accuracy in predicting charge transport. To address this problem, a robust method to construct artifact-free NCM (Figure S1, Supporting information) was developed, by implementing three loops of short MD simulations to screen the computational samples: (1) produce reasonable initial conditions with an artificial potential; (2) refine the structure with all bridges substituted by alkyl counterparts; (3) exclude samples with broken bonds during short runs in high temperature/pressure conditions (500 K/5 kbar). For the selected candidates, MD simulations were performed within the *NPT* ensemble at 500 K/5 kbar using a Nose/Hoover thermostat/barostat, with a time step of 0.5 fs for a period of 500 ps to mimic the conditions at the formation stage from geochemistry records,[25] which was then followed by an intermediate process for 500 ps, and then with another 500 ps simulation at 300–700 K/1 atm to represent operational conditions for future devices. The Large-scale Atomic/Molecular Massively Parallel Simulator package (LAMMPS)[26] was employed with all interactions described by the ReaxFF reactive force field,[27] which has shown reactivity trends in good agreement with quantum mechanics calculations and experimental data.[28] Each simulation cell is $35 \times 35 \times 35$ Å^3 containing ≈5000 atoms. The emergence of artifacts including dangling bonds and unrealistic bonding configurations was monitored by tracking the neighbor list of each atom.

Charge Hopping Rate: The artifact-free samples obtained by MD simulations were then used to explore electronic properties. The energy levels and reorganization energies of each fragment were calculated within the framework of density functional theory (DFT) as implemented in the SIESTA (v4.0) package.[29] A polarized double-ζ basis set[30] was used with Troullier–Martins pseudopotentials,[31] and the exchange-correlation energy was described by the PBE functional.[32] While the calculated transport variables depend on the choices of functional and basis set, such variations are acceptable based on the tests and thus will not qualitatively affect the conclusions (detailed validation is documented in Section SI, Supporting Information). The anticrossing method[33] was applied to compute electron couplings between fragments, with eigenvalues perturbed by external electric fields. This is quite challenging for the system because of the difficulty in searching minimum splitting points and the large amount of pairs (≈200) that must be considered in each network sample. An efficient algorithm to address this challenge by automatically tracking wavefunction localization and splitting variation was developed (Figure S2, Supporting information). A standard Brent's method was implemented with additional termination criteria: (1) distance between the centers of two relevant wavefunctions smaller than 0.5 Å; (2) variation among the set of smallest splittings smaller than 0.5 meV. Finally, the phonon-assisted charge-hopping rates were estimated by Marcus theory,[34] which was widely used to understand charge dynamics in disordered systems.[13a,35] Further discussion regarding the selection of charge transport model is provided in Section SI (Supporting Information).

Carrier Mobility: Once all the charge transfer rates between neighboring fragments are obtained (with the cutoff distance set as 10 Å, for nonbonded pairs), KMC simulations were performed until the diffusion distance was 2–3 orders of magnitude larger than the intermolecular spacing. The next position was selected randomly from the neighbors with a probability $P_n = k_{mn}/\sum k_{mn'}$ (m and n denote the current site and its neighbors), while the residence time was set to $1/\sum k_{mn}$.[21a] By averaging over 1000 trajectories, a linear relationship between the mean-square displacement (MSD) (r^2) and the diffusion time (t) was attained, which allowed to estimate the diffusion coefficient by $D = \frac{1}{2n}\lim_{t\to\infty}\frac{r(t)^2}{t}$ with the dimensionality factor $n = 3$. Finally, the charge mobility was evaluated by the Einstein relation $\mu = eD/k_BT$. Further details regarding the computational methods are provided in Section SA (Supporting Information).

Supporting Information

Supporting Information is available from the Wiley Online Library or from the author.

Acknowledgements

H.L. and T.Z. contributed equally to this work. The authors appreciate helpful discussions with Brent D. Keller, Mark Disko, Heather Elsen, and Hans Thomann. This work was supported by ExxonMobil under the MIT Energy Initiative (Grant No. EM09079). This research used resources of the National Energy Research Scientific Computing Center, a DOE Office of Science User Facility supported by the Office of Science of the U.S. Department of Energy under Contract No. DE-AC02-05CH11231. The authors acknowledge the support from the National Natural Science Foundation of China (11804403, 11832019) and the Natural Science Foundation of Guangdong Province (2018B030306036). This research used computational resources of the National Supercomputer Center in Guangzhou.

Conflict of Interest

The authors declare no conflict of interest.

Keywords

carrier transport, density functional theory, disordered materials, molecular connectivity network, natural carbonaceous materials

Received: May 28, 2019
Revised: July 4, 2019
Published online: July 23, 2019

[1] a) C. Zhu, R. E. Usiskin, Y. Yu, J. Maier, *Science* **2017**, *358*, eaao2808; b) Y. Sun, N. Liu, Y. Cui, *Nat. Energy* **2016**, *1*, 16071.
[2] J. Mao, Z. Liu, J. Zhou, H. Zhu, Q. Zhang, G. Chen, Z. Ren, *Adv. Phys.* **2018**, *67*, 69.
[3] B. Chanda, F. Bezanilla, *Neuron* **2008**, *57*, 345.
[4] G. Reguera, *Proc. Natl. Acad. Sci. USA* **2018**, *115*, 5632.
[5] M. Zander, *Chemistry and Properties of Coal Tar and Petroleum Pitch*, Universidad de Alicante, Alicante, Spain **2000**.
[6] L. H. Peebles, *Carbon Fibers: Formation, Structure, and Properties*, CRC Press, Boca Raton, FL **2018**.
[7] B. D. Keller, N. Ferralis, J. C. Grossman, *Nano Lett.* **2016**, *16*, 2951.
[8] a) R. Ye, C. Xiang, J. Lin, Z. Peng, K. Huang, Z. Yan, N. P. Cook, E. L. G. Samuel, C.-C. Hwang, G. Ruan, G. Ceriotti, A.-R. O. Raji, A. A. Marti, J. M. Tour, *Nat. Commun.* **2013**, *4*, 2943; b) C. Hu, C. Yu, M. Li, X. Wang, J. Yang, Z. Zhao, A. Eychmueller, Y. P. Sun, J. Qiu, *Small* **2014**, *10*, 4926; c) H. Shengliang, W. Zhijia, C. Qing, A. Trinchi, Y. Jinlong, *Appl. Surf. Sci.* **2016**, *378*, 402; d) S. R. Singamaneni, J. van Tol, R. Ye, J. M. Tour, *Appl. Phys. Lett.* **2015**, *107*, 212402.
[9] C. Bousige, C. M. Ghimbeu, C. Vix-Guterl, A. E. Pomerantz, A. Suleimenova, G. Vaughan, G. Garbarino, M. Feygenson, C. Wildgruber, F.-J. Ulm, R. J. M. Pellenq, B. Coasne, *Nat. Mater.* **2016**, *15*, 576.
[10] A. Troisi, *Chem. Soc. Rev.* **2011**, *40*, 2347.
[11] a) M. Van der Auweraer, F. C. De Schryver, P. M. Borsenberger, H. Bassler, *Adv. Mater.* **1994**, *6*, 199; b) Z. G. Yu, D. L. Smith, A. Saxena, R. L. Martin, A. R. Bishop, *Phys. Rev. B* **2001**, *63*, 085202.
[12] a) K. Shimakawa, K. Miyake, *Phys. Rev. B: Condens. Matter Mater. Phys.* **1989**, *39*, 7578; b) T. Tiedje, J. M. Cebulka, D. L. Morel, B. Abeles, *Phys. Rev. Lett.* **1981**, *46*, 1425.
[13] a) H. S. Li, D. Zhitomirsky, S. Dave, J. C. Grossman, *ACS Nano* **2016**, *10*, 606; b) T. Chen, K. V. Reich, N. J. Kramer, H. Fu, U. R. Kortshagen, B. I. Shklovskii, *Nat. Mater.* **2016**, *15*, 299; c) S. Lee, D. Zhitomirsky, J. C. Grossman, *Adv. Funct. Mater.* **2016**, *26*, 1554.
[14] a) N. Tessler, Y. Preezant, N. Rappaport, Y. Roichman, *Adv. Mater.* **2009**, *21*, 2741; b) P. M. Borsenberger, E. H. Magin, M. van der Auweraer, F. C. de Schryver, *Phys. Status Solidi A* **1993**, *140*, 9; c) M. Jaiswal, R. Menon, *Polym. Int.* **2006**, *55*, 1371.
[15] Y. Liu, N. Ferralis, L. T. Bryndzia, J. C. Grossman, *Carbon* **2016**, *101*, 361.
[16] S. Murata, M. Hosokawa, K. Kidena, M. Nomura, *Fuel Process. Technol.* **2000**, *67*, 231.
[17] a) J. P. Mathews, A. L. Chaffee, *Fuel* **2012**, *96*, 1; b) J. P. Mathews, A. C. T. van Duin, A. L. Chaffee, *Fuel Process. Technol.* **2011**, *92*, 718.
[18] P. W. M. Blom, M. J. M. de Jong, J. J. M. Vleggaar, *Appl. Phys. Lett.* **1996**, *68*, 3308.
[19] H. Sirringhaus, *Adv. Mater.* **2005**, *17*, 2411.
[20] W. Zhu, S. J. Singer, Z. Zheng, A. T. Conlisk, *Phys. Rev. E* **2005**, *71*, 041501.
[21] a) Z. Shuai, H. Geng, W. Xu, Y. Liao, J.-M. Andre, *Chem. Soc. Rev.* **2014**, *43*, 2662; b) H. S. Li, Z. G. Wu, M. T. Lusk, *J. Phys. Chem. C* **2014**, *118*, 46.
[22] H. Geng, Q. Peng, L. Wang, H. Li, Y. Liao, Z. Ma, Z. Shuai, *Adv. Mater.* **2012**, *24*, 3568.
[23] T. Petersen, I. Yarovsky, I. Snook, D. G. McCulloch, G. Opletal, *Carbon* **2004**, *42*, 2457.
[24] a) V. Fernandez-Alos, J. K. Watson, R. vander Wal, J. P. Mathews, *Combust. Flame* **2011**, *158*, 1807; b) F. Castro-Marcano, V. V. Lobodin, R. P. Rodgers, A. M. McKenna, A. G. Marshall, J. P. Mathews, *Fuel* **2012**, *95*, 35.
[25] W. J. Schopf, *Earth's Earliest Biosphere: Its Origin and Evolution*, Princeton University Press, Princeton, NJ **1983**.
[26] S. Plimpton, *J. Comput. Phys.* **1995**, *117*, 1.
[27] K. Chenoweth, A. C. T. van Duin, W. A. Goddard III, *J. Phys. Chem. A* **2008**, *112*, 1040.
[28] a) F. Castro-Marcano, A. M. Kamat, M. F. Russo Jr., A. C. T. van Duin, J. P. Mathews, *Combust. Flame* **2012**, *159*, 1272; b) A. Bagri, C. Mattevi, M. Acik, Y. J. Chabal, M. Chhowalla, V. B. Shenoy, *Nat. Chem.* **2010**, *2*, 581; c) E. Salmon, A. C. T. van Duin, F. Lorant, P.-M. Marquaire, W. A. Goddard III, *Org. Geochem.* **2009**, *40*, 1195.
[29] J. M. Soler, E. Artacho, J. D. Gale, A. Garcia, J. Junquera, P. Ordejon, D. Sanchez-Portal, *J. Phys.: Condens. Matter Mater. Phys.* **2002**, *14*, 2745.
[30] J. Junquera, O. Paz, D. Sanchez-Portal, E. Artacho, *Phys. Rev. B* **2001**, *64*, 235111.
[31] N. Troullier, J. L. Martins, *Phys. Rev. B: Condens. Matter Mater. Phys.* **1991**, *43*, 1993.
[32] J. P. Perdew, K. Burke, M. Ernzerhof, *Phys. Rev. Lett.* **1996**, *77*, 3865.
[33] I.-H. Chu, M. Radulaski, N. Vukmirovic, H.-P. Cheng, L.-W. Wang, *J. Phys. Chem. C* **2011**, *115*, 21409.
[34] R. A. Marcus, *Faraday Discuss. Chem. Soc.* **1982**, *74*, 7.
[35] M. B. Goldey, D. Reid, J. de Pablo, G. Galli, *Phys. Chem. Chem. Phys.* **2016**, *18*, 31388.

